PHYSICAL REVIEW A VOLUME 40, NUMBER 5 SEPTEMBER 1, 1989

Cryogenic-laser-fusion target implosion studies performed with the OMEGA uv-laser system

F. J. Marshall, S. A. Letzring, C. P. Verdon, S. Skupsky, R. L. Keck, J. P. Knauer,
R. L. Kremens, D. K. Bradley, T. Kessler, J. Delettrez, H. Kim,
J. M. Soures, and R. L. McCrory
Laboratory for Laser Energetics, University of Rochester, 250 East River Road, Rochester, New York 14623-1299

(Received 18 August 1988; revised manuscript received 27 December 1988)

A series of direct-drive laser-fusion implosion experiments was performed on cryogenically cooled, DT-filled glass microballoons with the OMEGA 24-beam uv (351-nm) laser system. The targets consisted of glass microballoons having radii of 100 to 150 μm, wall thicknesses of 3 to 7 μm, filled with DT gas at pressures of 75 to 100 atm. The targets were cooled to below the freezing point of DT, *in situ*, by a cryogenic target system. The targets were irradiated by approximately 1 to 1.2 kJ of uv light in 650-ps Gaussian pulses. The on-target irradiation uniformity was enhanced for these experiments by the use of distributed phase plates, which brought the estimated irradiation nonuniformities to $\sim 12\%$ (σ_{rms}). Target performance was diagnosed by an array of x-ray, plasma, and nuclear instruments. The measured target performance showed $\sim 70\%$ absorption, thermonuclear yields of 10^6 to 10^8 neutrons, and final fuel areal densities of 20 to 40 mg/cm^2 for the optimum targets examined in these experiments. Fuel densities at the time of thermonuclear neutron production, inferred from direct measurements of the fuel areal density, were in the range of 20 to 50 g/cm^3 (100 to 200 times the density of liquid DT) for the optimum targets.

I. INTRODUCTION

Direct-drive laser fusion is accomplished by uniformly illuminating spherical fuel-bearing pellets with high-power laser beams, causing their implosion and subsequent many-fold increase in density and temperature. Recently, short-wavelength lasers have been found to be capable of efficient compression of fusion pellets due to the creation of large ablation pressures (≥ 20 Mbar) by predominately collisional absorption.[1,2] Eventually, for inertial confinement fusion (ICF) to become an economical method for producing power, the gain (thermonuclear energy out divided by laser driver energy) must exceed ~ 100. It has been estimated that the DT fuel in such a pellet must be compressed to ~ 1000 times its liquid density (XLD) and reach a temperature of 4–5 keV in the central region for thermonuclear ignition and efficient burn to occur.[3]

In order to obtain efficient compression of a target, the fuel should initially be at a low temperature and be compressed adiabatically. If enough fuel is compressed in this way and heating of the central region of the fuel mass is obtained during the final stages of the implosion, then ignition of the fuel and a net gain of energy will occur. A way to achieve high compression of fusion fuel is to cryogenically cool the target so that the fuel initially forms a solid layer on the inside edge of the pusher. This, along with additional requirements such as pulse shaping and low radiative preheat, must be met in order to compress fusion fuel on a low adiabat, which is required for reactor-scale targets.

In this paper we describe direct-drive laser-fusion experiments performed on cryogenically cooled targets that were compressed by the short-wavelength (351-nm) beams of the OMEGA laser system. While not all of the necessary requirements for low-adiabat, nearly isentropic compression[4] are met in these experiments, the use of cryogenic targets is an important step in the study of the performance of targets designed to obtain high fuel densities. The targets used in these experiments consisted of simple glass microballoons filled with high-pressure DT gas. These targets were held in place on ultra-low-mass supports inside a cryogenically cooled housing positioned inside the OMEGA target chamber. The targets were prepared for an implosion experiment by the fast-refreeze technique[5] which optimizes the uniformity of the frozen fuel layer (to be discussed below).

Target performance was extensively characterized by a set of x-ray, plasma, and nuclear instruments. The x-ray and plasma diagnostics used included the following: plasma calorimeters, charge collectors, an x-ray calorimeter, an x-ray microscope, a high-speed four-frame x-ray framing camera, a streaked x-ray spectrograph, and a 3-GHz soft x-ray diode array. The compressed fuel conditions were diagnosed with neutron and particle detectors, including the following: a set of neutron detectors, a detector system for measuring the activation of target shell material by the thermonuclear neutrons,[6] fuel knock-on detectors and a set of neutron time-of-flight detectors.

Previous experiments with indirect-drive (x-ray driven) targets[7] have reported compressed fuel densities in the range of 50–120 XLD using nuclear activation techniques, which measure the areal density ($\rho\Delta R$) of the pusher material surrounding the compressed fuel. The compressed fuel densities were inferred from the measured $\rho\Delta R$ using the assumptions of mass conservation, a one-dimensional model of the compressed core, and pressure balance between shell and fuel. In contrast, the values of fuel ρR presented in this paper were measured directly. These measurements do not depend on values of shell areal density, temperature of the imploded material or amount of fuel-shell mixing; they are the first such direct measurements of highly compressed thermonuclear fuel.

II. EXPERIMENTS

A. Laser conditions

The OMEGA laser system is a 24-beam, frequency-tripled, Nd:glass laser system.[8] For the experiments described in this work the pulsed output was produced by an actively mode-locked oscillator.[9] Recent modifications of the OMEGA system include the use of liquid-crystal polarizers,[10] which enabled circularly polarized radiation to propagate through the entire front end of the amplifier system, thereby minimizing stress birefringence induced on the rod amplifiers, and the use of distributed phase plates[11] (DPP's) to increase the uniformity of the target irradiation.

Typically, the OMEGA system output was ~125 J per beam at 1054 nm in a ~750-ps pulse, full width at half maximum (FWHM), with a corresponding frequency tripled output per beam of ~75 J in a ~650-ps pulse (FWHM). Beam diameters were 17 cm (95% intensity) at the output of the frequency-tripling crystals. Individual beam energies were measured by reflection of a small fraction of the beam into integrating calorimeters which measured the 1ω, 2ω, and 3ω components of the conversion crystal output with a beam-to-beam accuracy of 1% and an absolute accuracy of 1–2 %. The beam-on-target arrival time was adjusted to be coincident to within 3 ps. The on-target energy for each beam was determined by measuring the loss in energy incurred as the beam propagated from the output of the conversion crystals into the target chamber. The variation in beam-to-beam energy was reduced to an average of ~5% ($\sigma_{\rm rms}$) for these experiments. The 24 beams of OMEGA were focused onto the target by $f/3.7$, 566-mm focal length, antireflection coated fused silica, aspherical, single element lenses. Individual beam pointing was verified to an accuracy of ~10 μm or less of lateral displacement from the target center and ~50 μm or less of transverse displacement from the target center.

The on-target illumination uniformity was enhanced for these experiments by incorporating a distributed phase plate into each beam before the final focus lens. The DPP's modify the phase front of the OMEGA beams (phase front errors have been found to be the dominant source of intensity nonuniformities at the target plane[12]) by shifting the phase of the beam by a randomly assigned amount of either 0 or π in approximately 10 000 hexagonally shaped subregions of the beam. The DPP's provide an improved target irradiation uniformity with a slight reduction (~20%) in the average energy on target. The actual variation in illumination uniformity has been estimated from measurements of the equivalent-target-plane intensity distribution produced when a DPP is placed in an OMEGA beam. Figure 1 shows the computed 24-beam superposition of intensities decomposed into spherical harmonic components. The variation in intensity uniformity due to DPP-modified OMEGA beams is computed to be ~8% ($\sigma_{\rm rms}$) with a relatively flat spectrum for spherical harmonic modes 2–60, assuming thermal smoothing in the plasma by 1% of the beam diameter (~3 μm). In actual experiments a larger variation in intensity uniformity occurs due principally to the beam-to-beam energy output variation [which was <9% ($\sigma_{\rm rms}$) for all of the experiments]. The combined varia-

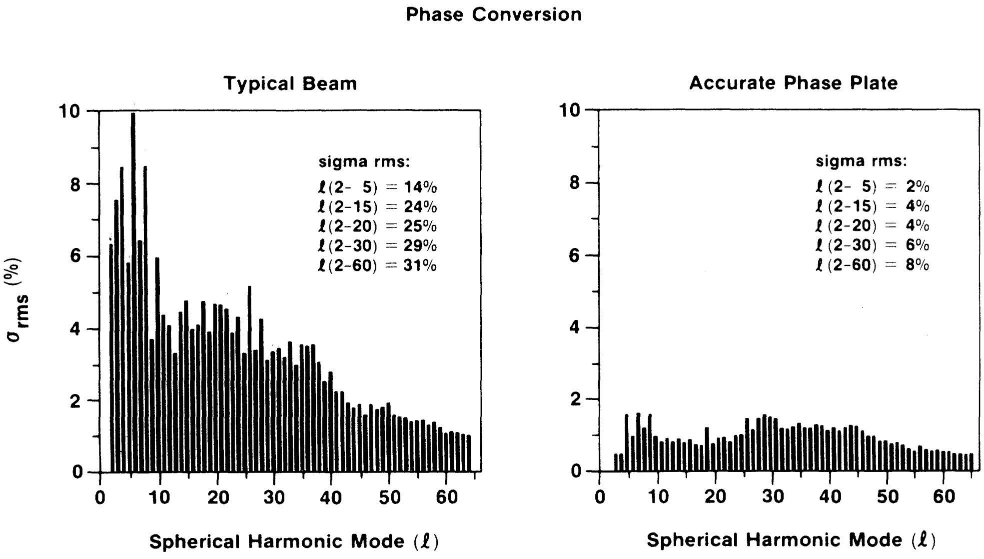

FIG. 1. Overall improvement in the irradiation uniformity on target is assessed by computing a 24-beam superposition of intensities and spherical harmonic decomposition. The intensity nonuniformity ($\sigma_{\rm rms}$%) is reduced by a factor of 6 for modes $l=2-20$, and by a factor of 4 for modes $l=2-60$. Smoothing by 1% of the beam diameter is assumed.

tion adds in quadrature, producing an estimated intensity fluctuation of $\lesssim 12\%$ ($\sigma_{\rm rms}$) for these experiments.

B. Targets

Implosion experiments were performed on glass microballoons containing near equimolar mixtures of DT at pressures of 75 and 100 atm. (The actual molar ratio of deuterium to tritium was measured at Mound Laboratories by a magnetic scanning cycloid mass spectrometer and found to be 0.86 ± 0.01 for the 100-atm targets.) Target diameters were measured to an accuracy of ± 5 μm and target wall thicknesses to an accuracy of ± 0.2 μm. The targets were mounted, using no glue, on a support structure which was compatible with the cryogenic target-positioning system.[13] The targets were supported by spider silks (~ 0.5 μm in diameter) drawn across a U-shaped copper mount whose width (3 mm) and thickness (100 μm) were constrained by the requirement that the U-mount be narrow enough to fit in the liquid-He-cooled target shroud and thin enough so as not to obscure the converging OMEGA beams (Fig. 2). A target was assembled onto its mount by placing it on a cradle consisting of two spider silks, after which additional spider silks (1–3) were placed over and under the target in order to hold it in place. Finally, the target-mount assembly was coated with 0.2 μm of parylene in order to give it additional mechanical stability.

C. Cryogenic target system

Targets mounted as described above were positioned and cooled to below the freezing point of DT (~ 19 K) by the OMEGA cryogenic target-positioning system (cryogenic system), which is described in detail in Ref. 13. A schematic diagram of the cryogenic system is shown in Fig. 3. It consists of four major subsystems: (1) a liquid-He-cooled target positioner; (2) a fast retractable liquid-He-cooled shroud; (3) a heating laser system used to rapidly vaporize the frozen fuel while the target is inside the cooled shroud; and (4) a shearing interferometer system used to document the frozen-fuel layer thickness and uniformity.

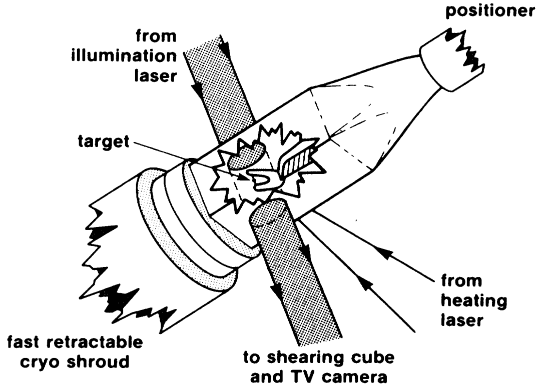

FIG. 2. Schematic of the target assembly as it would appear positioned inside the cooling shroud. The heating laser and interferometer system are used to optimize the solid DT layer thickness uniformity.

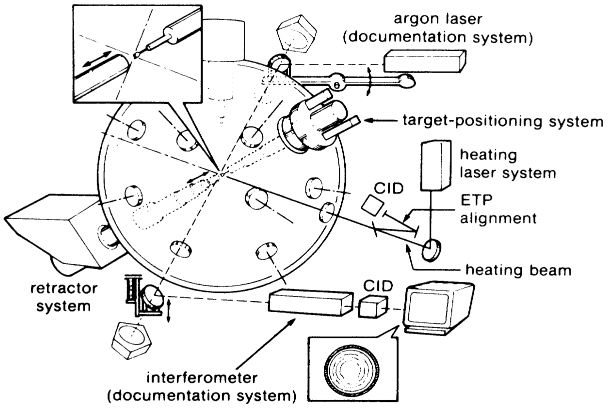

FIG. 3. OMEGA cryogenic target positioning system schematic.

Preparation of the cryogenic target is based on the fast-refreeze technique originally pioneered by Musinski *et al.*[5] The sequence of steps necessary to ready a target for an implosion experiment in the OMEGA target chamber was as follows: The target was placed in the vacuum system through the air lock of the target positioner, after which cooling of the positioner was initiated by inserting into it a liquid-He transfer line. After the target mount and cryostat reached temperature equilibrium, contraction of the target-mount assembly ceased and the target was then moved to the tank center (to within 10 μm). Next, the retractable liquid-He-cooled shroud was positioned over the target-mount assembly. A seal was formed by the open end of the shroud pressing against a stack of polyester washers (attached to the face of the target-positioner cryostat). Vapor phase He, flowing out of an orifice in the base of the shroud, provided the additional cooling necessary to solidify the DT fuel in a layer on the inner surface of the glass shell. The shroud also shielded the target from the infrared radiation emitted by the room-temperature OMEGA target chamber. The cooling rate was controlled to some degree by varying the gap between the shroud and the positioner, the minimum attainable gap (~ 100 μm) giving the maximum internal vapor pressure and therefore the maximum cooling rate. A typical operating condition pressure was measured to be 3 mTorr of He inside the shroud.

Final target preparation required interactive use of the interferometer and heating laser to redistribute the frozen-fuel layer into the most uniform layer possible. [An argon-ion laser having an output of 10 mW at 488 nm was used in the interferometer and an argon-ion laser having an output of 6 W (multiline) was used to heat the target.] This was accomplished by a trial and error sequence where the relative uniformity of the fuel was inferred by visual examination of the interferogram symmetry. If a nonuniform fuel layer was observed, an example of which is shown in Fig. 4(a), then the fuel layer was vaporized by a short pulse (~ 0.5 sec) from the heating

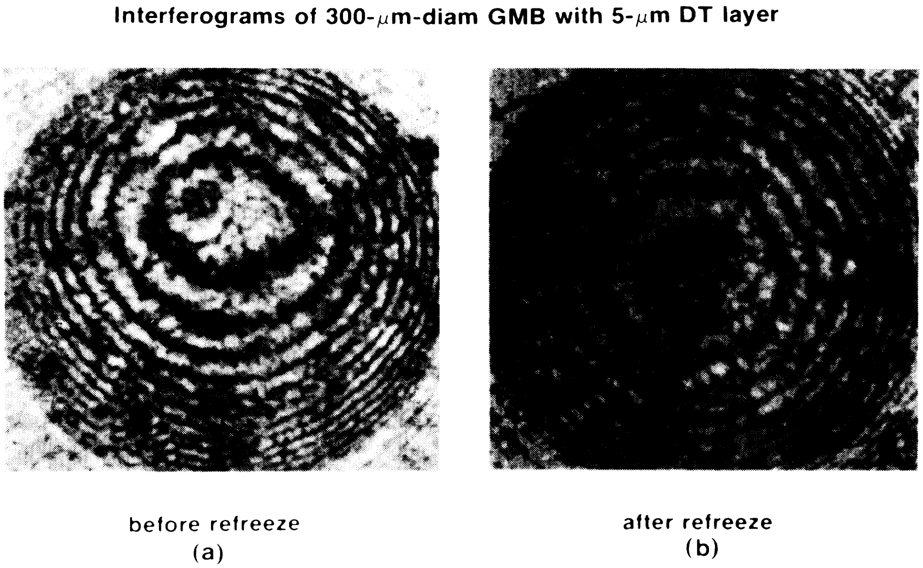

FIG. 4. Interferograms of a 300-μm-diam glass microballoon before (a) and after (b) preparation by the fast-refreeze technique. The prepared target (b) has a nearly uniform solid DT layer with a thickness of 5 μm.

laser, after which point the fuel rapidly reformed into a frozen layer. This was continued, while adjusting heating laser beam pointing and focusing until a near uniform interferogram pattern was obtained [Fig. 4(b)]. Estimates of the precision to which the uniformity of the fuel layer could be measured with this technique were made by ray-tracing simulation. These simulations indicated that symmetry of the interferogram to within 0.5 fringes implied a fuel layer uniformity with $\leq 20\%$ variation in layer thickness. (This was about the limit to which variations could be detected interactively; it is representative of the uniformity of the initial fuel layer in the implosion experiments.) The target temperature was measured indirectly by a thermocouple attached to the cooling shroud. It typically registered a temperature of between 6 and 8 K before shroud retraction. The targets are presumed to have been in near temperature equilibrium with the cooling shroud since the turbulent gaseous helium provided an excellent path for heat conduction. Finally, ~40 ms before target irradiation, the cooling shroud was rapidly retracted. The target was left exposed to the ambient environment for ~10 ms before illumination occurred allowing time for the shroud to retract out of the path of the laser beams. The length of time required for the DT to melt was > 30 ms for the targets used in these experiments. The approximate melting time was determined by videotaping a retraction sequence and noting on playback that the frozen layer fringe pattern was maintained for more than one video frame (33 ms). No additional significant source of heat, such as amplified spontaneous emission (ASE) arriving before the main laser pulse, was present at the time of laser illumination. Estimates of the total ASE present imply a total integrated energy incident on target prior to the main pulse of ~1 μJ, which is insufficient to melt the target even with 100% absorption (the actual fractional absorption should be $\ll 1\%$).

D. Target design

Target design and prediction of target performance was carried out with the one-dimensional (LILAC) and two-dimensional (ORCHID) hydrodynamic simulation codes. Both of these codes use tabular equation of state (SESAME),[14] flux-limited electron thermal transport, multifrequency group radiation transport with local thermodynamic equilibrium (LTE) opacities[15] and inverse-bremsstrahlung-absorption energy deposition through a ray-tracing algorithm in the underdense plasma. A flux limiter, $f=0.06$ with a sharp cutoff, was used in the simulations described in this work. This value of the flux limiter was found to give the best agreement between measured and predicted fractions of the incident uv light absorbed by the target and the absorbed energy converted to x rays by the target.[16] These previous experiments were performed on both solid and hollow glass spheres. Implosion experiments performed with gas-filled glass targets have shown good agreement between the measured and predicted shell radius versus time when this same flux limiter is used.[17]

Figures 5(a)–5(f) show the LILAC calculated target behavior for a typical cryogenic experiment. In this example, the target is a 150-μm inner radius (R_0) glass microballoon having a 5-μm wall (ΔR_0) and containing 100 atm of DT frozen into a 5-μm ice layer. The target is irradiated with 1200 J of uv radiation in a 650-ps (FWHM) Gaussian pulse. Figures 5(a) and 5(b) show the fuel-shell interface trajectory and the time history of the in-flight aspect ratio ($R/\Delta R$), respectively. Initially, the shell is compressed, reaching an aspect ratio of ~70 at ~500 ps before the peak of the pulse, followed by a continuous

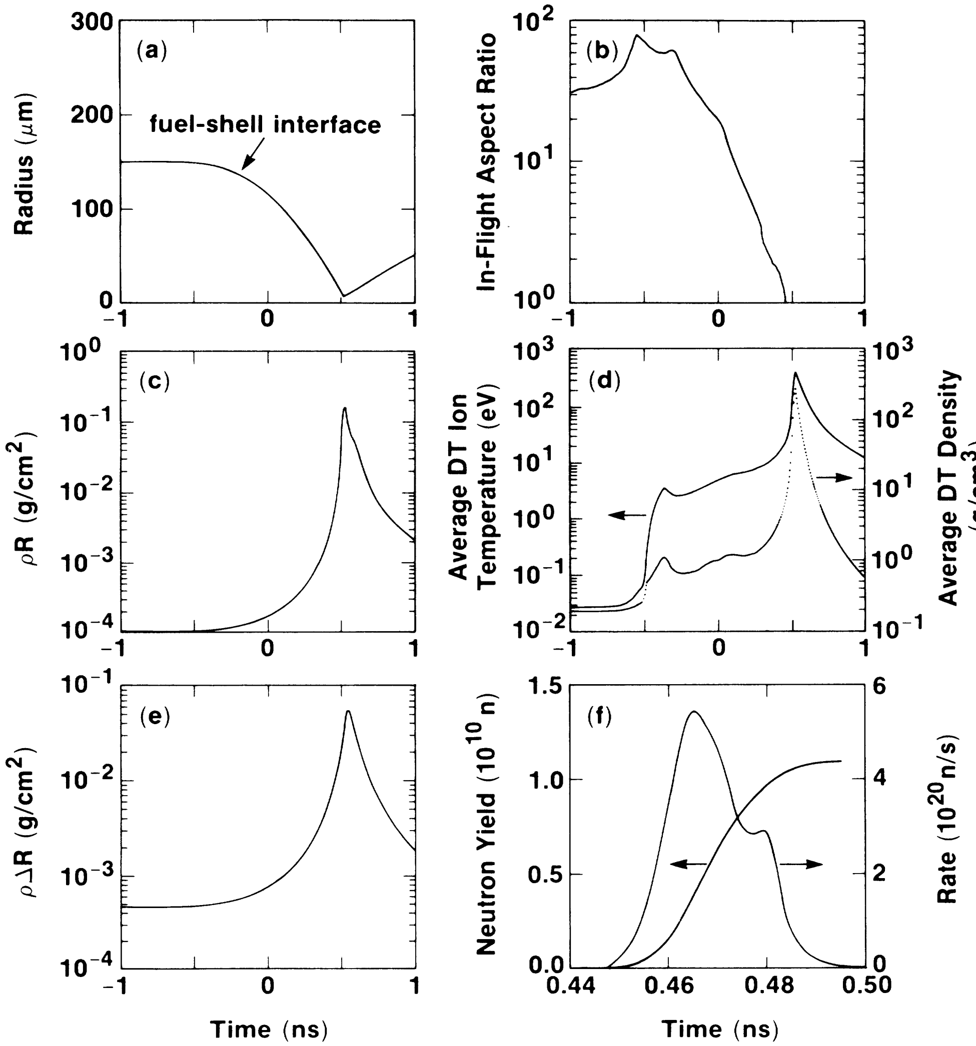

FIG. 5. One-dimensional hydrocode simulations (LILAC) of the implosion of a 300-μm-diam, 5-μm wall, glass microballoon having a 100-atm DT fill which has been cryogenically cooled forming a 5-μm solid DT layer. (a) The fuel-shell interface trajectory. (b) The inflight aspect ratio. (c) The fuel areal density. (d) The fuel temperature and density. (e) The shell areal density. (f) The integrated yield and rate of generation of neutrons during the time of peak compression. Times are with respect to the peak of the laser pulse.

decompression of the shell, due to radiative heating, as the implosion progresses. The fuel and shell begin to accelerate rapidly at ~400 ps before the peak of the pulse, the fuel density (ρ) rises to a peak value of ~300 g/cm^3 and an average ion temperature (T_i) of 0.5 keV is reached during the stagnation phase [Fig. 5(d)]. Peak fuel and shell areal densities, [Figs. 5(c), 5(e)] ρR and $\rho \Delta R$, are ~150 and ~50 mg/cm^2, respectively. A neutron yield of 1.1×10^{10} is obtained within a 40-ps time interval with the peaks in the rate coinciding with the time of fuel coalescence at the origin and peak compression, respectively [Fig. 5(f)]. The fuel region reaches a minimum predicted size of 7 μm in radius corresponding to a convergence ratio of 22. (The convergence ratio C_R is defined as the initial fuel-pusher interface radius divided by the minimum fuel-pusher interface radius.) The average fuel density during the time of neutron production (neutron-averaged ρ) is 210 g/cm^3, which is lower than the peak density of 300 g/cm^3. The other neutron-averaged quantities are $\langle T_i \rangle_n = 1.2$ keV, $\langle \rho R \rangle_n = 140$ mg/cm^2, and $\langle \rho \Delta R \rangle_n = 36.0$ mg/cm^2.

E. Results

Cryogenic target experiments were performed on a large number (~100) of DT-filled glass microballoons. The optimum conditions for target performance and performance characterization were determined experimentally. The most successful, well-diagnosed target experiments were obtained for glass microballoons filled with 100 atm of DT, having radii of 100–150 μm and shell thicknesses of 3–7 μm. Table I lists the target parameters, laser conditions, and measured target performance, along with LILAC predictions of performance, for those target experiments performed under optimum conditions, where the calculated convergence ratio exceeded 20, and for which values of the fuel areal density were obtained. (The optimum conditions include the use of DPP modified OMEGA beams and web-mounted targets which underwent a cryogenic-layer refreeze.) As will be shown below, targets with the highest calculated C_R also obtained the highest inferred fuel densities.

Time-resolved x-ray diagnostics measured the state of the shell material during the course of the implosion. Figure 6 shows a set of images taken by an x-ray framing camera.[18] The framing camera consisted of a pinhole camera assembly with an array of pinholes (17–18 μm in diameter) illuminating a gated microchannel plate (MCP). The pinhole images had a magnification of 10 and a resolution of $\sim 20\ \mu$m. Four x-ray images (frames) were obtained by four independently gated regions of the MCP with short (~ 300 ps) high-voltage pulses. The sensitive time of each frame was ~ 150 ps (FWHM) and the frames were separated by 250 ps. There is some spatial smearing in these framed images due to target motion; nevertheless, a ring of emission is seen, with the radius of this emission corresponding to the average shell radius during the frame. Figure 7 shows the measured and predicted radius of peak x-ray emission as determined from framed x-ray images for three target experiments for which the target wall thicknesses were 3, 5, and 6 μm.

Further information about the implosion time history was obtained from measurements taken with the MINIFLEX soft x-ray photodiode system.[19] The MINIFLEX system consists of an array of four x-ray sensitive photodiodes whose signals are read out by 3-GHz oscilloscopes, yielding spatially integrated time-resolved (~ 200 ps FWHM) measurements of the x-ray emission. Figure 8 shows the time-resolved x-ray emission observed with MINIFLEX for the three target experiments of Fig. 7 together with LILAC predictions of the MINIFLEX response. The measured and predicted curves were compared by normalizing the heights of the broad peak in the emission curve (corresponding roughly to the peak of the laser pulse) and by assuming that these peaks coincide in time. We observe that (a) the times of the measured and predicted stagnation peaks [Figs. 8(a), 8(b), and 8(c)] are nearly coincident and (b) the height of the measured stagnation peak appears to be slightly lower than predicted for the thicker targets. To summarize the time-resolved x-ray measurements: The size of the imploding shell as a function of time, measured by the x-ray framing camera, and the time of shell stagnation, measured by the MINIFLEX system, are in good agreement with the one-dimensional code predictions.

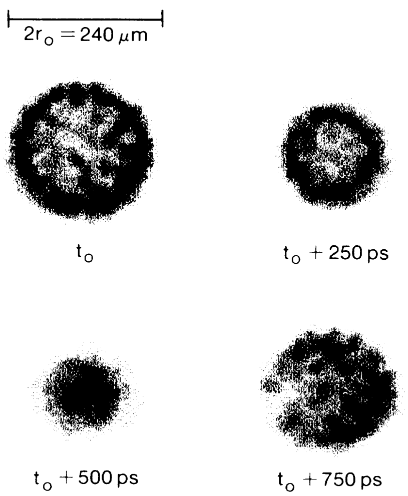

FIG. 6. X-ray images of a cryogenic target implosion taken with a four frame x-ray framing camera. The darker shaded regions are the regions of highest x-ray emission. Small scale structure is due principally to noise from the MCP.

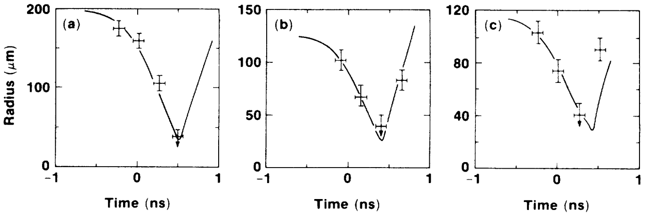

FIG. 7. Radius of peak x-ray emission vs time of three cryo targets having (a) 3-μm, (b) 5-μm, and (c) 6-μm walls determined from framed x-ray images and LILAC predictions of the same. Times are with respect to the peak of the laser pulse.

The total thermonuclear yield Y_N was measured for these experiments by Cu- and Ag-activation systems, and by an array of neutron scintillator-photomultiplier pairs.[20] All of these yield measuring systems were cross calibrated to the absolutely calibrated Cu-activation system. Errors in the measured yield for these experiments were due primarily to counting statistics. The actual yields obtained ranged from 10^6 to 10^8. Representative neutron yields obtained from experiments on high convergence ratio targets are given in column (8a) of Table I. Figure 9 shows the normalized neutron yield (the measured neutron yield divided by the calculated yield) plotted as a function of the calculated convergence ratio. The normalized yields range from 3×10^{-3} to 10^{-4}. The normalized neutron yields observed in previous gas-phase target experiments performed on OMEGA (Refs. 21–23) (see Fig. 9) ranged from nearly 1 for low C_R to $\sim 10^{-2}$ at a C_R of 23 for low-pressure-fill targets (10 atm). Previous high-pressure-fill (50 atm) gas-phase targets exhibited a more rapid fall off of neutron yield at higher C_R. The normalized neutron yields obtained in the cryogenic target experiments fall below the best performing gas-phase target experiments, but are above the trend seen for the higher-pressure-fill targets.

Routine measurements of the neutron velocity spectrum were made by the technique of time of flight. However, the flux levels were, in general, insufficient to provide accurate ion temperature information. Often only an upper limit could be placed on T_i ($\lesssim 1$ keV being typical for these experiments). Measurements of the shell areal density ($\rho\Delta R$) were made by the technique of Si activation[6,22] using an enhanced debris collector having an

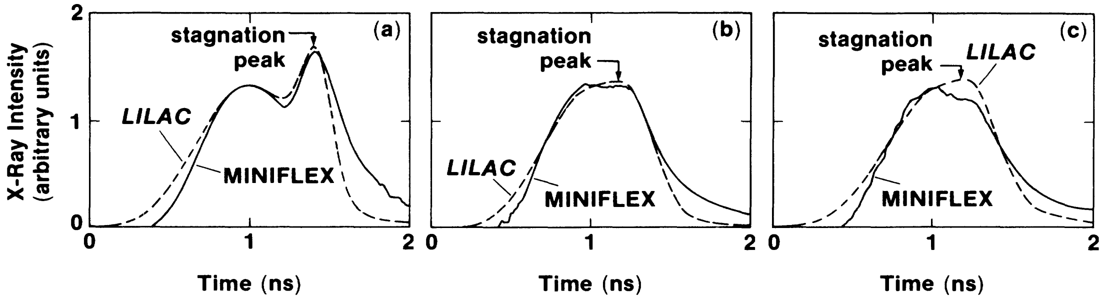

FIG. 8. Time-resolved spatially integrated x-ray fluence from cryo targets which have wall thicknesses of (a) 3 μm, (b) 5 μm, and (c) 6 μm and LILAC prediction of the same.

efficiency of 10%. Due to the difficulty of deploying this diagnostic technique, no measurements of $\rho\Delta R$ were obtained simultaneously with the more relevant measurements of fuel areal density (ρR). Details of these measurements will, therefore, not be presented in this work.

The fuel areal density ρR at the time of neutron yield (neutron-averaged fuel ρR) was measured by the "knock-on" diagnostic technique.[24–27] This technique measures the number of deuterons and tritons in the compressed fuel that are scattered by 14.1-MeV fusion neutrons, the number of such ions (knock-ons) being directly proportional to the fuel ρR. The ions were detected by stacks of polycarbonate (CR-39) track-detector foils with metallic filters in front of and in between the foils. The CR-39 foils used in these experiments were 150 μm thick. Three sets of knock-on detector foil-filter stacks were positioned at nearly mutually orthogonal positions around the target, both to increase collection solid angle and to provide as representative a sample of the average knock-on flux as possible. (When summed together, the knock-on detectors subtended a solid angle of ~1% of 4π for these experiments.) Deuterons and tritons were distinguished from other particles (e.g., protons) by counting only tracks with diameters exceeding a specified minimum diameter which completely penetrated an individual foil.[26,27]

The track selection criteria[26,27] which distinguishes fuel knock-ons from background protons resulted in sensitivity to deuterons in the energy range from 4.6 to 6.8 MeV and tritons in the range from 5.4 to 10.3 MeV. The addition of moderating material in front of the foils (both thin metal filters and other CR-39 foils) yielded sensitivity to deuterons and tritons with higher energies. The calculated energy bands and the filter-foil combinations used to obtain these bands are tabulated in Table II. Each foil samples a different portion of the knock-on spectrum. For values of the total areal density $\rho R_{\mathrm{tot}} \leq 50$ mg/cm^2 ($\rho R_{\mathrm{total}} = \rho R + \rho\Delta R$), the knock-on spectrum depends only on ρR, $\rho\Delta R$, and the known n-D, n-T scattering cross sections.[28] Figure 10 shows calculated knock-on spectra for both a low ρR_{total} and a moderate ρR_{total} case from a five-energy-band sample. For the low-density case

TABLE I. Summary of the results of high calculated convergence ratio ($C_R > 20$) cryogenic target experiments on 100 atm DT-filled glass microballoons (GMB's). The columns are (1) the OMEGA shot number; (2) the microballoon shell inner radius R_0 (μm); (3) the shell thickness ΔR_0 (μm); (4) the incident energy E_{inc} (J); (5a) the measured and (5b) the predicted absorbed energy E_{abs} (J); (6) the beam balance σ_{rms} (% rms); (7) the LILAC predicted convergence ratio C_R; (8a) the measured and (8b) the predicted thermonuclear neutron yield Y_N with the numbers in parentheses indicating the power of 10; (9a) the measured and (9b) the predicted neutron-averaged fuel areal density $\langle\rho R\rangle_n$ (mg/cm^2); and (10a) the inferred and (10b) the predicted neutron-averaged fuel density $\langle\rho\rangle_n$ (g/cm^3).

				(5a)	(5b)			(8a)	(8b)	(9a)	(9b)	(10a)	(10b)
	(2)	(3)	(4)	E_{abs}		(6)	(7)	Y_N		$\langle\rho R\rangle_n$		$\langle\rho\rangle_n$	
(1) Shot	R_0 (μm)	ΔR_0 (μm)	E_{inc} (J)	Expt. (J)	LILAC	σ_{rms} (%)	C_R LILAC	Expt. n_0's	LILAC	Expt. mg/cm^2	LILAC	Expt. g/cm^3	LILAC
16054	120	4.9	1080	747	780	4.9	23.1	9.6±0.2(6)	1.4(10)	30±5	96	27±6	158
16105	110	6.1	1066	768	828	8.7	22.2	4.0±0.7(6)	6.2(9)	40±13	68	50±24	107
16212	134	5.0	1138	858	875	7.4	24.4	6.4±0.8(6)	1.2(10)	29±8	130	22±9	216
16265	111	5.8	951	751	698	8.5	21.6	4.9±0.7(6)	6.5(9)	26±12	65	26±17	99
16266	137	5.7	1145	926	935	6.9	22.7	8.4±0.8(6)	1.7(10)	26±6	97	18±7	132
16267	134	5.8	1150	862	927	5.1	22.5	8.5±0.9(6)	1.6(10)	32±7	90	26±9	122
16268	134	5.7	1207	891	955	3.7	22.8	7.7±0.8(6)	1.9(10)	23±8	94	15±8	131
16270	103	5.2	1015	658	622	3.8	22.9	5.6±0.8(6)	6.1(9)	18±6	69	16±8	123
16272	118	7.0	1146	794	878	3.7	20.6	4.7±0.8(6)	5.4(9)	9±7	66	5±5	92
16279	128	5.9	1137	941	896	3.9	22.3	1.1±0.1(7)	1.4(10)	14±5	82	8±5	113

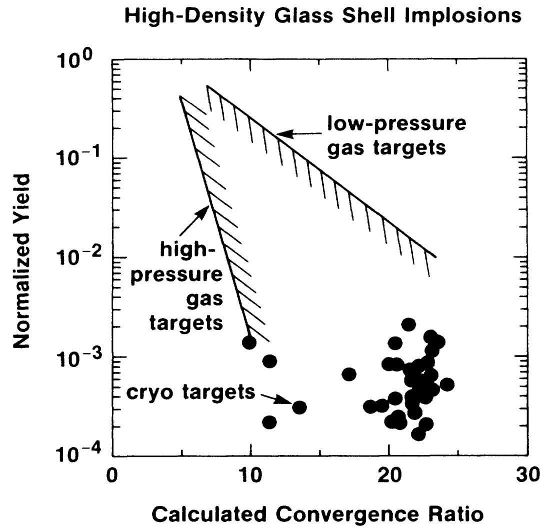

FIG. 9. Normalized neutron yield (ratio of experimentally measured yield to predicted yield) vs the calculated target convergence ratio (the ratio of the initial to final fuel-shell interface radius) for the cryogenic target experiments. The shaded region shows the range of normalized yields found for previous gas-phase glass pusher experiments.

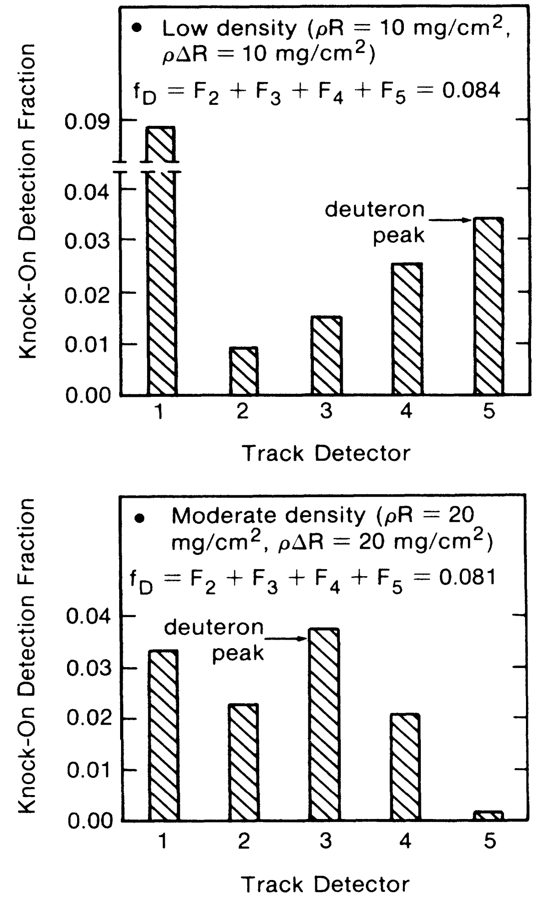

FIG. 10. Relative number of knock-ons in each of the five CR-39 foils for $\rho R_{\text{total}}=20$ mg/cm² and $\rho R_{\text{total}}=40$ mg/cm². Each foil is preceded by different amounts of moderating material to bring different parts of the knock-on spectrum into the foil's energy window. For deuterons (D) and tritons (T), the knock-on energy range (MeV) detected by each foil is shown in Table II. For $\rho R \gtrsim 5$ mg/cm², all tritons will have slowed down below ~9.8 MeV, so that only deuterons will produce tracks in the energy window for foils 2–5.

($\rho R_{\text{total}}=20$ mg/cm²) the high-energy peak of the deuteron spectrum (produced from near head-on collisions between neutrons and deuterons) lies in the window of foil 5, while for the moderate-density case ($\rho R_{\text{total}}=40$ mg/cm²) the deuteron peak has shifted to foil 3. We found that, although the position of the high-energy deuteron peak and hence the fraction of the total number of deuterons detected in any one foil differs depending on the amount of slowing down in the target, the sum of the knock-ons detected in foils 2–5 is nearly a constant fraction of the total; $f_D=0.085$, to within ±5%, for $\rho R_{\text{total}} \le 50$ mg/cm². (The fuel temperature, pusher temperature, and amount of fuel-shell mixing have only a small effect on the high-energy part of the deuteron spectrum which is detected here.) For higher ρR_{total} (>50 mg/cm²), the high-energy deuteron peak is sufficiently slowed down in the target that the peak begins to move out of these foils, and the fraction of the spectrum detected falls below 0.085. Thus the value $f_D=0.085$ represents an upper limit on the knock-on fraction, which is independent of conditions within the target. The relationship between knock-on counts and fuel ρR is[26]

$$\rho R = 1.08\times 10^3 \frac{K_D}{Y_N}\left[\frac{4\pi}{\Delta\Omega}\right]\frac{1}{f_D}\left[\frac{2\gamma+3}{\gamma}\right],$$

in mg/cm², where K_D is the sum of the knock-on tracks detected in foils 2–5, $\Delta\Omega$ is the solid angle subtended by

TABLE II. Knock-on detector foil-filter configuration.

Foil	Filter	Deuteron range E_{min} (MeV)	E_{max} (MeV)	Triton range E_{min} (MeV)	E_{max} (MeV)
1	25-μm Ta	6.3	8.2	7.3	10.6[a]
2	25-μm Ta+150-μm CR-39	8.2	9.9	9.8	10.6[a]
3	50-μm Ta+150-μm CR-39	9.5	11.0		
4	25-μm Ta+300-μm CR-39	9.9	11.3		
5	50-μm Ta+300-μm CR-39	11.0	12.4		

[a] The maximum recoil energy which can be obtained in an elastic collision with a 14.1-MeV neutron is 12.5 MeV for a deuteron and 10.6 for a triton assuming both are initially at rest.

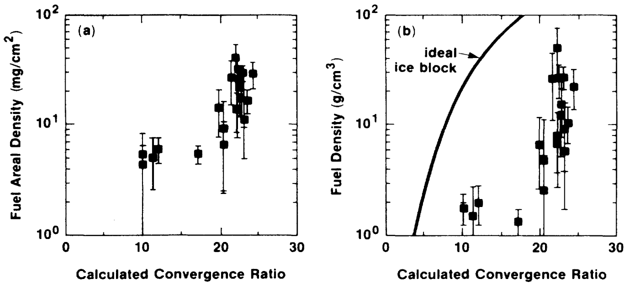

FIG. 11. (a) The measured fuel areal densities and (b) the inferred neutron-averaged fuel densities. The line in (b) indicates the maximum density which could be obtained for a given convergence ratio.

the foils, Y_N is the neutron yield, f_D is the fraction of the knock-on spectrum which falls in the energy window of foils 2–5, and γ is the deuterium-tritium molar ratio. Using $f_D=0.085$, an accurate estimate of ρR is obtained for $\rho R_{\text{total}} \leq 50$ mg/cm^2; for higher ρR_{total}, a lower bound on ρR is obtained, since f_D appears in the denominator of this expression.

Figure 11(a) shows the measured fuel areal densities plotted versus the calculated convergence ratios. Values of the measured fuel ρR for the optimum targets listed in Table I are given in column 9(a). The uncertainty of the values of ρR are calculated from the relative uncertainties in measurement of the knock-on flux and the neutron yield, which are added in quadrature. (The errors are dominated by the statistical uncertainty in the number of knock-on tracks detected.) The highest values of fuel ρR are in the range 20–40 mg/cm^2 which were obtained by targets with calculated convergence ratios in excess of 20. The number of knock-on counts obtained from these experiments ($\lesssim 40$) precluded a meaningful determination of the angular variation of the knock-on flux or the detailed shape of the knock-on spectrum.

The neutron-averaged fuel density can be estimated from the measured ρR by assuming a simple model for the distribution of the fuel. One such model (the "ice-block" model) assumes that the fuel has a constant density and is compressed into a region of radius R and that neutrons are produced at the center of this region.[29] Assuming that all of the initial mass of the fuel M is compressed into this region, the fuel density can be expressed as

$$\rho=(4\pi/3M)^{1/2}(\rho R)^{3/2} .$$

The fuel densities inferred from the measured ρR, using the ice-block model, are shown in Fig. 11(b). The highest inferred fuel densities are in the range of 20–50 g/cm^3 (100–200 XLD) again obtained with targets whose calculated convergence ratios are in excess of 20 [Table I, column 10(a)]. The curve in Fig. 11(b) shows the density that would be obtained if all of the fuel were to be uniformly compressed to the calculated convergence ratio (assuming 100 atm initial fuel pressure). This represents the maximum density which could be measured under ideal conditions, whereas the measured densities represent the average fuel density at the time of neutron production.

III. DISCUSSION

The amount of energy absorbed by the cryogenic targets was measured and found to be in good agreement with the predicted absorbed energy (Sec. II, Table I). The cryogenic target implosion velocities were diagnosed by measurements of the shell size versus time determined from x-ray framing camera images and by measuring the time of shell stagnation from x-ray photodiode measurements. These measurements indicate that, in the acceleration phase, target drive energetics are in reasonable agreement with LILAC simulations. The measured neutron yields [Table I, col. 8(a)] and the measured fuel areal densities [Table I, col. 9(a)], however, fall below the predicted values. It has been pointed out previously[22] that the falloff of neutron yield with increasing convergence ratio could be explained by illumination nonuniformities of the OMEGA system. As is seen in Fig. 9 the cryogenic target experiments show a degradation in the neutron yield relative to one-dimensional predictions indicating that the performance of those targets may have been degraded by a similar mechanism. We note that the cryogenic targets have the additional complexity of a fuel layer which may be nonuniform in thickness due to imperfections in the target preparation technique. Two-dimensional (ORCHID) simulations of the effect of low-order-mode ($l \leq 2$) cryogenic layer thickness variations, up to twice the experimentally observed values, result in less than a factor of 2 yield reduction from one-dimensional simulations assuming perfect illumination uniformity. Initial two-dimensional calculations indicate that the effect of the estimated OMEGA illumination nonuniformities on target performance dominate those caused by fuel or shell thickness variations.

The presence of nonuniform illumination during the target implosion could cause a reduction in target performance via the following related mechanisms.

(1) Development of shell distortions during the acceleration phase (due to illumination nonuniformities or target thickness nonuniformities) may have resulted in the mixing of pusher material into the fuel during the acceleration phase and departures from spherical symmetry during the deceleration and stagnation phase of the implosion with additional mixing of pusher material into the fuel region.

(2) The mixing of pusher material into the fuel, as well as the associated asymmetries, would be expected to reduce the final fuel temperatures (and yield) due to increased cooling by radiation and increased conduction surface area as well as a less efficient conversion of kinetic energy into internal energy.

A possible consequence of pusher distortion and/or fuel-pusher mixing would be a modification of the neutron emission history from that predicted. This modification could result in sampling the fuel when it is at a lower density. As shown in Fig. 5(c), the fuel areal density is predicted to increase by more than an order of magnitude within a very short amount of time during the deceleration and stagnation phases (~ 50 ps). Since the fuel areal density determined by the knock-on technique is neutron weighted, small variations in the temporal history of the neutron emission could significantly change the measured fuel areal density.

A possible scenario to explain the reduction in the observed fuel areal density from that predicted would be as follows: Neutron production begins at approximately the time predicted by one-dimensional simulations. The neutron production rate begins to rise but is rapidly quenched due to the mechanisms discussed above. This quenching effectively moves the peak in the neutron production to an earlier time resulting in a lower measured fuel areal density.

To date, we have no direct experimentally determined evidence for the presence of material mixing other than the observed reductions in the neutron yield and areal density compared to simulations. Its presence and effect on the performance of these targets as well as methods to improve the illumination uniformity and cryogenic target quality are under active investigation at this time.

IV. SUMMARY

A series of direct-drive ablatively driven implosion experiments were carried out on the 24-beam, 351-nm, OMEGA laser system using cryogenic DT glass microballoons. Distributed phase plates were used to improve the target irradiation uniformity. Typical measured absorption fractions of 60–80% agreed with predicted values. Time-resolved x-ray measurements showed that the shell radius versus time and the time of shell stagnation were in good agreement with one-dimensional simulations. These results indicate that the acceleration phase of the implosion is being accurately modeled by one-dimensional simulations. Deviations from one-dimensional performance were more apparent during the stagnation and burn phases, for example, (a) the height of the x-ray stagnation peak, (b) the neutron yield, and (c) the fuel areal density. It is likely, although not certain, that these effects are due to nonuniform implosion of fuel and shell material caused by residual nonuniformities in the OMEGA laser irradiation on target. Nevertheless, fuel areal densities of 20–40 mg/cm^2 were measured using the knock-on diagnostic technique, implying neutron-averaged fuel densities of 20–50 g/cm^3 (100–200 XLD). These experiments have resulted in the first direct measurements of the fuel areal density of highly compressed fusion fuel that do not involve any assumptions about temperature or fuel-shell mixing. The inferred fuel densities are the highest attained for any direct-drive laser fusion experiments.

ACKNOWLEDGMENTS

The authors acknowledge the support of the Laser Operations group, Experimental group, Target Fabrication group, and staff of the Laboratory for Laser Energetics. The targets and the cryogenic system used in this study were supplied by KMS Fusion, Inc. Lawrence Livermore National Laboratory supplied the x-ray framing camera. Los Alamos National Laboratory supplied the MINIFLEX soft x-ray diode system. This work was supported by the U.S. Department of Energy Office of Inertial Fusion under Agreement No. DE-FC03-85DP40200 and by the Laser Fusion Feasibility Project at the Laboratory for Laser Energetics which has the following sponsors: Empire State Electric Energy Research Corporation, New York State Energy Research and Development Authority, Ontario Hydro, and the University of Rochester.

---

[1] R. S. Craxton, R. L. McCrory, and J. M. Soures, Sci. Am. **255**, 68 (1986).

[2] R. L. McCrory, J. M. Soures, C. P. Verdon, P. Audebert, D. Bradley, J. Delettrez, R. Hutchison, S. D. Jacobs, P. Jaanimagi, R. Keck, H. Kim, J. Knauer, R. Kremens, S. Letzring, F. Marshall, P. McKenty, M. C. Richardson, A. Simon, R. Short, S. Skupsky, and B. Yaakobi, in *High Intensity Laser-Matter Interaction,* Proceedings of the Society of Photo-Optical Instrumentation Engineers (SPIE, Bellingham, WA, 1988), Vol. 913; Laboratory for Laser Energetics Annual Report 1987, No. DOE/DP 40200-64, 1988 (unpublished), pp. 93–106.

[3] J. Nuckolls, L. Wood, A. Thiessen, and G. Zimmerman, Nature (London) **239**, 139 (1972).

[4] R. F. Kidder, Nucl. Fusion **16**, 3 (1976).

[5] D. L. Musinski, T. M. Henderson, R. J. Simms, and T. R. Pattinson, J. Appl. Phys. **51**, 1394 (1980).

[6] M. C. Richardson, R. F. Keck, S. A. Letzring, R. L. McCrory, P. W. McKenty, D. M. Roback, J. M. Soures, C. P. Verdon, S. M. Lane, and S. G. Prussin, Rev. Sci. Instrum. **57**, 1737 (1986).

[7] Lawrence Livermore National Laboratory, Livermore, CA, Laser Program Annual Report 1984, Report No. UCRL-50021-84, 1985 (unpublished).

[8] J. M. Soures, R. J. Hutchison, S. D. Jacobs, L. D. Lund, R. L. McCrory, and M. C. Richardson, in *Proceedings of the 10th Symposium on Fusion Engineering, Philadelphia, 1983* (IEEE, New York, 1983), p. 1392.

[9] Laboratory for Laser Energetics LLE Review **23**, Quarterly Report No. DOE/DP40200-03, 1985 (unpublished), pp. 109–115.

[10] S. D. Jacobs, K. A. Cerqua, T. J. Kessler, W. Seka, and R. Bahr, in *16th Annual Symposium on Optical Materials for High Power Lasers, Boulder, CO, 1984,* Natl. Bur. Stand. (U.S.) Spec. Publ. No. 727 (U.S. GPO, Washington, D.C., 1986), pp. 15–22.

[11] Laboratory for Laser Energetics LLE Review **33**, Quarterly Report No. DOE/DP40200-65, 1987 (unpublished), pp. 1–10.

[12] S. Skupsky and T. Kessler, Opt. Commun. (to be published); Laboratory for Laser Energetics LLE Review **31**, Quarterly Report No. DOE/DP40200-47, 1987 (unpublished), pp. 106–113.

[13] Laboratory for Laser Energetics LLE Review **33**, Quarterly Report No. DOE/DP40200-65, 1987 (unpublished), pp.

11–18.

[14] B. I. Bennett, J. D. Johnson, G. I. Kirley, and G. T. Rand, Los Alamos National Laboratory Report No. LA-7130, 1978 (unpublished).

[15] W. F. Huebner, A. L. Merts, N. H. Magee, Jr., and M. F. Argo, Los Alamos National Laboratory Report No. LA-6760-M, 1977 (unpublished).

[16] Laboratory for Laser Energetics LLE Review **31**, Quarterly Report No. DOE/DP40200-47, 1987 (unpublished), pp. 101–106.

[17] G. G. Gregory, P. A. Jaanimagi, P. W. McKenty, S. A. Letzring, and M. C. Richardson, in *High Speed Photography, Videography, and Photonics V,* Proceedings of the Society of Photo-Optical Instrumentation Engineers (SPIE, Bellingham, WA, 1987), Vol. 832, p. 383.

[18] J. D. Kilkenny, P. Bell, R. Hanjks, G. Power, R. Turner, J. Weidwald, and D. K. Bradley, Rev. Sci. Instrum. (to be published).

[19] G. Pien, M. C. Richardson, P. D. Goldstone, R. H. Day, F. Ameduri, and G. Eden, Nucl. Instrum. Methods Phys. Res. B **18**, 101 (1986).

[20] M. C. Richardson, R. F. Keck, S. A. Letzring, R. L. McCrory, P. W. McKenty, D. M. Roback, J. M. Soures, C. P. Verdon, S. M. Lane, and S. G. Prussin, Rev. Sci. Instrum. **57**, 1737 (1986).

[21] Laboratory for Laser Energetics LLE Review **28**, Quarterly Report No. DOE/DP40200-26, 1986 (unpublished), pp. 155–163.

[22] Laboratory for Laser Energetics LLE Review **31**, Quarterly Report No. DOE/DP40200-47, 1987 (unpublished), pp. 93–100.

[23] Laboratory for Laser Energetics LLE Review **25**, Quarterly Report No. DOE/DP40200-19, 1985 (unpublished), pp. 7–19.

[24] S. Kacenjar, L. M. Goldman, A. Entenberg, and S. Skupsky, J. Appl. Phys. **56**, 2027 (1984).

[25] S. Skupsky and S. Kacenjar, J. Appl. Phys. **52**, 2608 (1981).

[26] S. Kacenjar, S. Skupsky, A. Entenberg, L. Goldman, and M. Richardson, Phys. Rev. Lett. **49**, 463 (1982).

[27] S. Kacenjar, Doctoral thesis, University of Rochester, 1982.

[28] ENDF/D-IV Library, National Neutron Cross Section Center, Brookhaven National Library [described in Brookhaven National Laboratory Report No 50274 (1970)].

[29] E. M. Campbell, W. M. Ploeger, P. H. Lee, and S. M. Lane, Appl. Phys. Lett. **36**, 965 (1980).

Interferograms of 300-μm-diam GMB with 5-μm DT layer

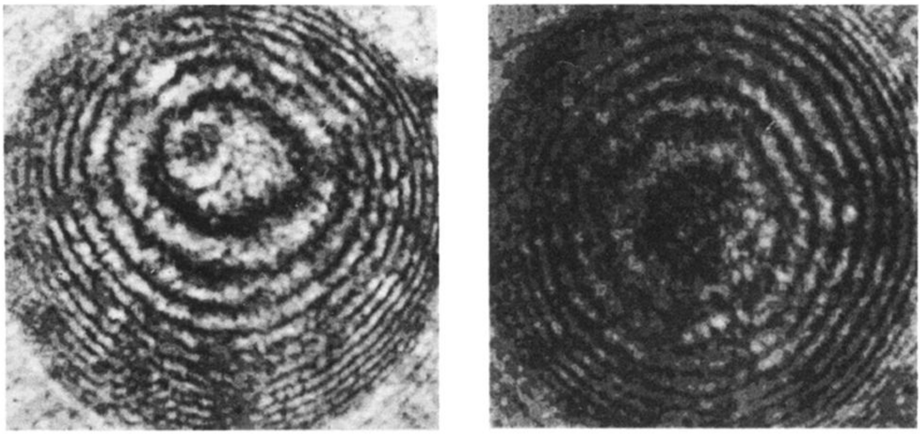

before refreeze
(a)

after refreeze
(b)

FIG. 4. Interferograms of a 300-μm-diam glass microballoon before (a) and after (b) preparation by the fast-refreeze technique. The prepared target (b) has a nearly uniform solid DT layer with a thickness of 5 μm.